Surface-patterned chalcogenide glasses with high-aspect-ratio microstructures for long-wave infrared metalenses

Zhaofeng Gu[1,2], Yixiao Gao[1,2]*, Kongsi Zhou[1,2], Junyang Ge[1,2], Chen Xu[1,2], Lei Xu[3], Mohsen Rahmani[3], Ran Jiang[4], Yimin Chen[1,2], Zijun Liu[1,2], Chenjie Gu[1,2], Yaoguang Ma[5], Jianrong Qiu[5] and Xiang Shen[1,2,4,6]*

Multidimensional-engineering chalcogenide glasses is widely explored to construct various infrared photonic devices, with their surface as a key dimension for wavefront control. Here, we demonstrate direct patterning high-aspect-ratio microstructures on the surface of chalcogenide glasses offers an efficient and robust method to manipulate longwave infrared radiations. Despite chalcogenide glass being considered soft in terms of its mechanical properties, we successfully fabricate high-aspect-ratio micropillars with a height of 8 μm using optimized deep etching process, and we demonstrate a 2-mm-diameter all-chalcogenide metalens with a numerical aperture of 0.45 on the surface of a 1.5-mm-thick As_2Se_3 glass. Leveraging the exceptional longwave infrared (LWIR) transparency and moderate refractive index of As_2Se_3 glass, the all-chalcogenide metalens produces a focal spot size of ~$1.39\lambda_0$ with a focusing efficiency of 47% at the wavelength of 9.78 μm, while also exhibiting high-resolution imaging capabilities. Our work provides a promising route to realize easy-to-fabricate, mass-producible planar infrared optics for compact, light-weight LWIR imaging systems.

Keywords: chalcogenide glasses; long wave infrared; metalens

Introduction

Chalcogenide glasses are a type of amorphous material composed of elements from the chalcogen group (sulfur, selenium, or tellurium), which hold significant importance in infrared optics due to their broad transparent window ranging from the near to longwave infrared wavelengths[1]. Various engineering techniques have been developed to transform chalcogenide glasses into infrared optical components. For instance, these glasses can be drawn into optical fibers, offering promising applications in mid-infrared lasers[2] and supercontinuum generation[3]. Patterned chalcogenide films, produced

[1]Laboratory of Infrared Materials and Devices, Research Institute of Advanced Technologies, Ningbo University, Ningbo 315211, China; [2]Zhejiang Key Laboratory of Advanced Optical Functional Materials and Devices, Ningbo 315211, China; [3]Advanced Optics & Photonics Laboratory, Department of Engineering, School of Science and Technology, Nottingham Trent University, Nottingham NG11 8NS, United Kingdom; [4]Faculty of Electrical Engineering and Computer Science, Ningbo University, Ningbo 315211, China; [5]State Key Laboratory of Extreme Photonics and Instrumentation, College of Optical Science and Engineering; International Research, Center for Advanced Photonics, Zhejiang University, Hangzhou 310027, China; [6]Ningbo Institute of Oceanography, Ningbo 315832, China.

*Correspondence: YX Gao, E-mail: gaoyixiao@nbu.edu.cn; X Shen, E-mail: shenxiang@nbu.edu.cn

Received: 22 April 2024; Accepted: 17 July 2024; Published online: 3 September 2024

This is an early view version and will be formally published in a coming issue with other articles in due time.

through thermal evaporation and etching processes, have found applications in on-chip nonlinear optics for all-optical signal processing and sensors[4,5]. Gradient-index chalcogenide glass, utilizing glass-composition-dependent refractive index[6,7], offers a novel approach for correcting chromatic aberrations in imaging systems[8]. Moreover, owing to their low glass transition temperature, chalcogenide glasses are well-suited for molding procedure, enabling cost-effective production of infrared lenses[9]. In addition to these bulk engineering methods, the surface of chalcogenide glasses also offers a crucial platform for engineering infrared optics, allowing for the creation of diffractive optical elements[10] and microlenses[11] using techniques such as precision glass molding or femtosecond laser processes. However, the aforementioned chalcogenide micro/nanostructures typically have an aspect ratio near 1 or lower. Considering that chalcogenide glasses are generally susceptible to brittle fracture, fabricating high-aspect-ratio microstructures on the chalcogenide glass surface remains a challenge.

Metasurface, consisting subwavelength artificial structures arranged in two-dimensional periodic array, offers an intriguing platform for full control of light wave[12−15], which have been widely explored in quantum optics[16], all-optical computing[17], optical cryptography[18], etc. As a typical metasurface specialized on phase manipulation, dielectric metalenses can focus light with the advantages of compact size, light weight, potential for integration with other optical components, which rely on high-aspect-ratio microstructures to manipulate wavefront[12,19−20]. Through meticulous design of both the individual microstructures and their spatial arrangement, diffraction-limited achromatic imaging performance could be achieved within a single piece of dielectric metalens. Typically, dielectric metalenses are fabricated using heterogeneous dielectric structures, i.e. high refractive index structures for phase manipulation and low refractive index substrate for mechanical support[12]. Heterogeneous metalenses demonstrate impressive performance across shorter wavelength ranges, spanning from visible to mid-infrared frequencies[21−26]. However, efficient phase control for longwave infrared light necessitates thick microstructure layers, often approaching the scale of the leveraging the exceptional longwave infrared (LWIR) wavelength (~10 μm). Fabricating such thick microstructures on a heterogeneous substrate poses significant challenges, including the potential for cracking or structural instabilities, arising from incompatible ther-

mal expansion coefficients between different materials, which may deteriorate the mechanical stability of metalenses under varying ambient conditions. Direct patterning of metasurfaces onto transparent dielectric surfaces[21,27,28] is a viable solution to address the challenges associated with heterogeneous metalenses in LWIR. Fan et al. demonstrate an all-silicon LWIR metalens efficiently focusing a CO_2 laser beam at 10.6 μm[29]. Later works are dedicated to achieving large area[30] and large viewing angles[31] in all silicon LWIR metalenses. Despite the well-established fabrication capabilities of the silicon platform, a noteworthy drawback of silicon stems from its inherent material loss—particularly significant absorption beyond 7 μm[32]. This characteristic stands as a limiting factor in the pursuit of high-efficiency all-silicon metalenses in the LWIR regime. Germanium is an appealing LWIR material due to its low absorption loss within the LWIR spectrum. Wang et al. utilize all germanium metalens for LWIR light focusing[33]. However, the large refractive index of germanium introduces substantial reflection losses at the air-germanium interface, which requires an additional antireflection layer to mitigate this issue[34]. Furthermore, the large temperature coefficient of refractive index (dn/dT) of germanium gives rise to pronounced focal shifts in response to changes in ambient temperature, potentially degrading imaging quality in practical applications.

In this paper, we demonstrate all-chalcogenide metalenses for LWIR imaging by directly patterning the surface of a chalcogenide glass. Employing an optimized deep etching process, chalcogenide micropillars with a height of 8 μm and varying diameters sitting on the same material are successfully prepared for efficient transmission wavefront control, despite chalcogenide glasses being soft in terms of their mechanical properties. Benefiting from the excellent LWIR transmittance of As_2Se_3 glasses, the fabricated all-chalcogenide metalenses demonstrate diffraction-limited focusing characteristics and high-resolution LWIR imaging performances. Compared to heterogeneous counterparts, the single-material (monolithic) LWIR metalens offer enhanced mechanical robustness and simplified fabrication processes. These advantages, including ease of fabrication and potential for mass production, position them as promising candidates for compact LWIR imaging devices.

Results and discussion

Properties of chalcogenide glass
We first show the advantages of chalcogenide glass

As$_2$Se$_3$ as the material for homogeneous LWIR metalenses. As$_2$Se$_3$ glasses demonstrate extremely low loss in the long-wave infrared band and low-temperature coefficient of refractive index (dn/dT), which have been widely explored in mid/long infrared applications ranging from optical fibers to thermal imaging lenses. Figure 1(a) shows a photo of a homemade and double-sided polished As$_2$Se$_3$ disk. We prepared As$_2$Se$_3$ glass disks with a diameter of 10 mm using single point diamond turning (SPDT) manufacturing technique (Nanoform X, Ametek Inc., USA) followed by a polishing process to ensure the high-parallelism and smoothness of the glass surfaces. Figure 1(b) shows the AFM images of the surface of as-prepared As$_2$Se$_3$ glass disks. The average surface roughness (R_a) and mean square roughness (R_q) are 0.52 nm and 0.71 nm, respectively, indicating a surface smooth enough for subsequent processing. Figure 1(c) shows the measured transmittance of common LWIR materials. Here, CaF$_2$, BaF$_2$, ZnS, ZnSe, Si, and Ge substrates are double-side polished with a thickness of 1 mm, while the As$_2$Se$_3$ disk has a thickness of 1.5 mm. The transmittance spectra of different LWIR materials are measured by a Fourier transform infrared (FTIR) spectrometer (Perkin-Elmer, Spectrum 100). The corresponding refractive index of these materials are summarized in Table 1. We could observe that substrate with a higher refractive index yields a lower average transmittance owing to larger Fresnel reflection, as depicted in Fig. 1(c), and the reflection losses would have a negative impact on the overall efficiency of metalenses. It should be noted that using antireflection coating on the structured surface may alleviate this[34]. However, it poses additional fabrication challenges. In addition, clear absorption peaks could be observed for the Si substrate, which is another key factor deteriorating the efficiency of all-silicon metalenses[29,35]. As for fluoride materials (such as CaF$_2$ and BaF$_2$), the reflection loss could be suppressed, however, the low refractive index of these materials requires a large aspect-ratio microstructure to obtain entire 2π phase coverage. ZnS and ZnSe are popular LWIR materials with wideband infrared transparency and moderate refractive index, while currently these materials face difficulties for etching, especially for microstructures with micrometer-scale height applied in LWIR metalenses. Chalcogenide glass, including As$_2$Se$_3$, have excellent LWIR transparency. Figure 1(d) shows the
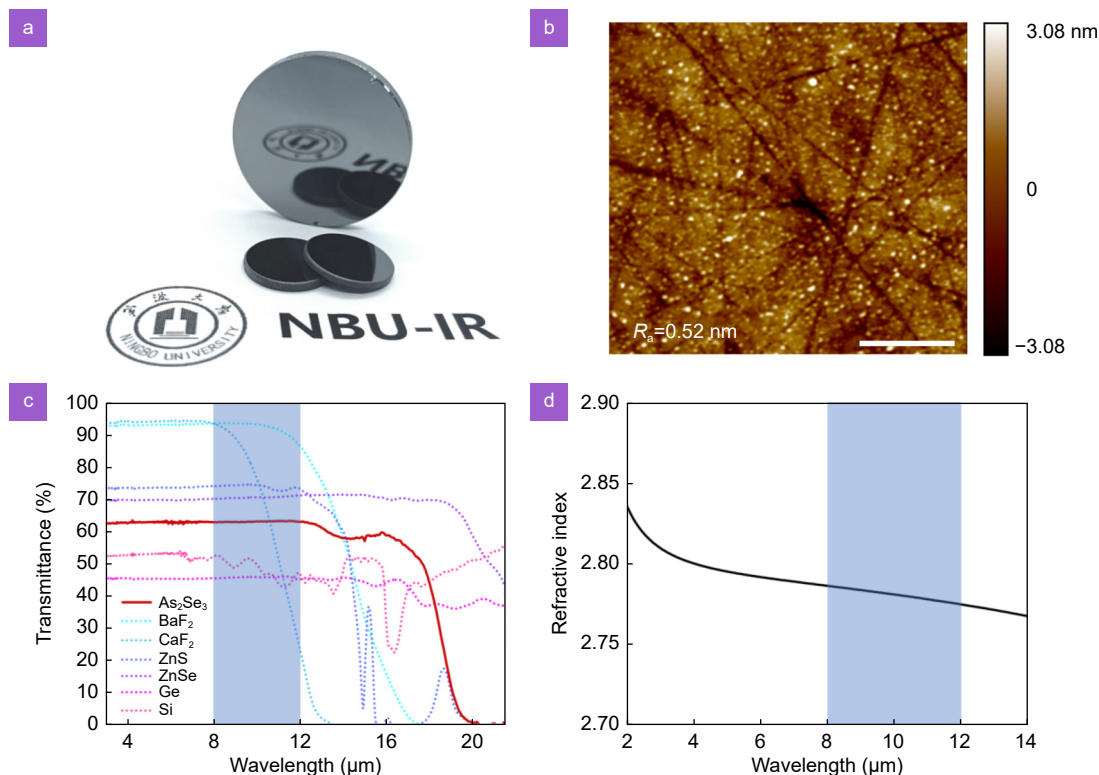
Fig. 1 | (a) Photo of double-side polished As$_2$Se$_3$ disks. **(b)** Two-dimensional AFM image of a polished As$_2$Se$_3$ disk, Scale bar: 1 μm. **(c)** Transmission spectra of common LWIR materials. The thickness of all samples is 1 mm, except for the As$_2$Se$_3$, which has a thickness of 1.5 mm. The blue shaded region indicates the LWIR band ranging from 8 to 12 μm. **(d)** The refractive index of As$_2$Se$_3$ glass as a function of wavelength.

Table 1 | Properties of As$_2$Se$_3$ glass compared with other long-wave infrared materials.

Materials	Refractive index (at ~9.78 µm)	Transmittance[a] (at 9.78 µm)	dn/dt (×10^{-6} K^{-1})	Vickers hardness[b] (HV)	Expansion coefficient (×10^{-6} K^{-1})
As$_2$Se$_3$	2.78	63.2%	32	145	20.6
CaF$_2$	1.31[36]	80.0%	−11.5[37]	172	18.5[38]
BaF$_2$	1.40[39]	93.6%	−14.5[39]	87	18.1[38]
ZnS	2.20[40]	74.6%	46.3[41]	167	17.2[42]
ZnSe	2.41[36]	70.7%	52[41]	112	12.7[42]
Si	3.42[40]	51.2%	150[43]	~1050	2.64[44]
Ge	4.00[40]	46.0%	400[43]	~800	5.9[45]

(a) Data measured by FTIR spectrometer.

(b) Data measured by Vickers hardness tester.

refractive index of As$_2$Se$_3$ glass in the infrared frequencies, obtained through an infrared ellipsometer (J. A. Woollam IR-VASE Mark II). In the LWIR region, As$_2$Se$_3$ glass demonstrate a moderate refractive index, e.g. 2.78 @ 9.78 µm, and the material dispersion is low as well, as denoted by the blue shaded area in Fig. 1(d). Moreover, its refractive index temperature coefficient is significantly lower than that of Si and Ge, resulting in good thermal stability under large temperature changes. Furthermore, although the thermal expansion coefficient of As$_2$Se$_3$ is higher than that of Si and Ge, it is comparable to other LWIR materials and is still in a small degree, which indicates that the structure expansion will not be large at high temperatures. These properties highlight As$_2$Se$_3$ glass as an ideal base medium for the preparation of homogeneous LWIR metalenses.

Chalcogenide glasses are usually regarded as being soft in terms of mechanical properties, compared with other materials. We measured the hardness of As$_2$Se$_3$ disk as well as other materials using Vickers hardness tester (MH-3, Hengyi Co., China), summarized in Table 1. It could be observed that the hardness of As$_2$Se$_3$ is much lower than Si and Ge, indicating a soft mechanical properties of chalcogenide glasses, and we will later show that high-aspect-ratio microstructures could be achieved on As$_2$Se$_3$ glass using an optimized fabrication process.

Design of all-chalcogenide glass LWIR metalens

Next, we present the design process of LWIR metalens based on all-chalcogenide glass microstructures. Here, we utilize the simple but effective local phase modulating unit cell: As$_2$Se$_3$ micropillars with varying diameters arranged in square lattices, which also features polarization insensitivity, as depicted in Fig. 2(a). The height and diameter of the micropillars are denoted as H and D, respectively, and the period is represented by P along both

the x and y directions, as shown in Fig. 2(b). Figure 2(c-d) show the transmittance and phase delay as functions of the height and diameter of micropillars with light incident from the substrate side. It can be observed that phase delay experiences large variation upon diameter changing and would have full 2π coverage when H is large enough. Diameter changing also results in transmittance fluctuations, which influences the overall focusing efficiency of metalenses.

To achieve a high transmittance as well as full 2π phase coverage, we choose $P = 5.5$ µm and $H = 8$ µm. Figure 2(e) shows the corresponding transmittance and phase modulation curve as a function of diameter varying from 1.8 µm to 4.5 µm. We would like to emphasize here the average transmittance is mainly determined by the refractive index of the substrate. Therefore, compared with silicon- and germanium-based LWIR metalenses, a lower refractive index of As$_2$Se$_3$ helps to increase the average transmittance due to a lower reflection loss. Then, we select eight micropillars with different diameters as the metalens design units, i.e. the diameters are 2.00, 2.36, 2.58, 2.74, 2.93, 3.21, 3.59, and 4.12 µm, respectively, and micropillars with diameters from this library would introduce linear phase delay ranging from 0 to $7\pi/4$ with $\pi/4$ increment, as depicted in Fig. 2(f). The average transmittance of these 8 micropillars with different diameters is 74.8%.

When incident light impinges on the unit cell, each As$_2$Se$_3$ micropillar could be regarded as a truncated waveguide, where guided modes oscillate back and forth, forming a Fabry-Perot-like resonance. As depicted in Fig. 2(g), we plot three typical field profiles in one unit cell with different diameters, and the fields have different node numbers, indicating the different phase delay capabilities induced by the diameter modulation. Here, we consider the wavelength of the incident light to be
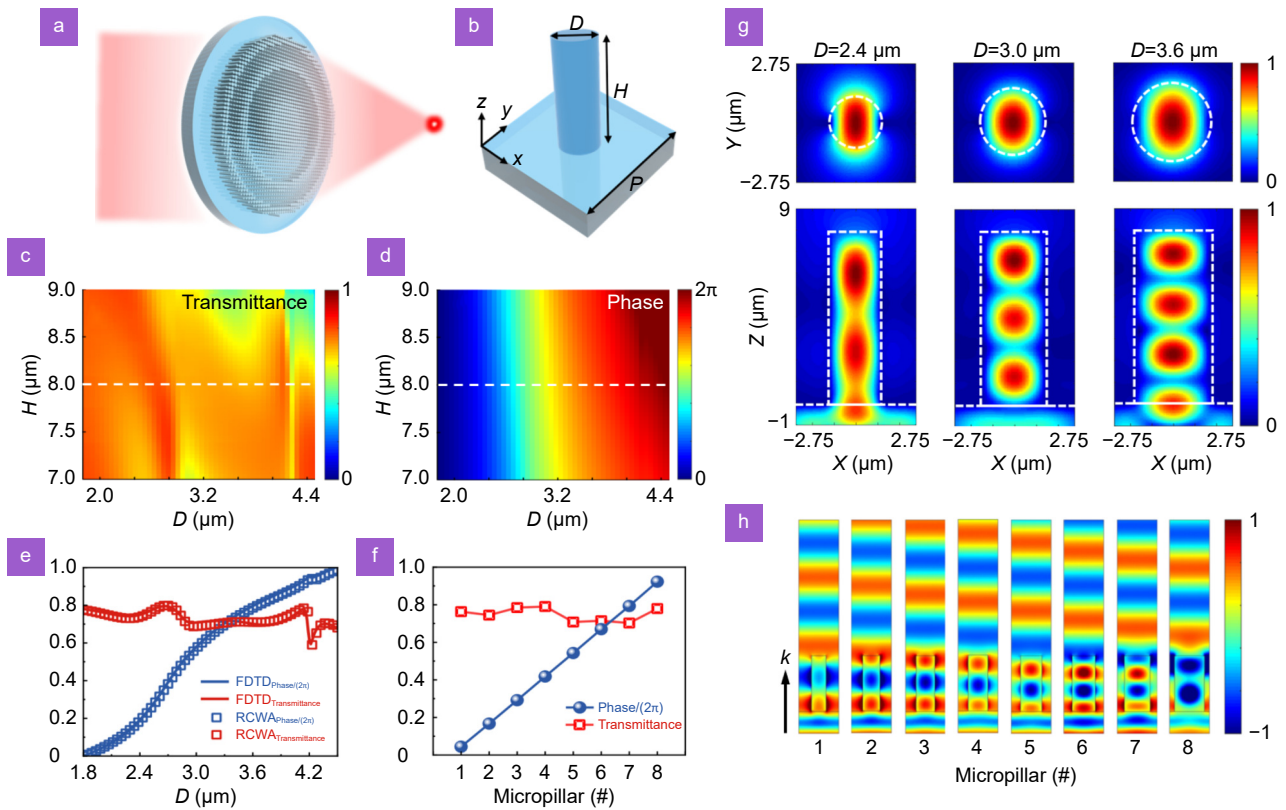
Fig. 2 | (a) Schematic for LWIR all-chalcogenide metalens operating in transmission mode. **(b)** Side view of the homogeneous metalens unit cell (As$_2$Se$_3$ micropillar on As$_2$Se$_3$ substrate with square lattice). **(c, d)** Transmission and phase diagrams as a function of the micropillar diameter D and height H at the wavelength of 9.78 μm, with a lattice constant P of 5.5 μm. **(e)** The transmission and phase of micropillar with different diameters were calculated at a lattice constant of P = 5.5 μm and a height of H = 8 μm. **(f)** The transmittance and phase of eight selected micropillars, which can provide high transmittance and equidistant phase shifts covering the entire 2π range. **(g)** The normalized field profiles in As$_2$Se$_3$ micropillars with diameters (i) D = 2.4 μm, (ii) D = 3.0 μm, and (iii) D = 3.6 μm. The white dashed lines outline the micropillar structure and the electromagnetic field is tightly confined within the cylindrical structure. **(h)** The transmitted electric field in one unit cell with selected micropillar diameters, corresponding to 2(f).

9.78 μm, where the refractive index of As$_2$Se$_3$ is 2.78. The underlying physics is that the effective mode index n_{eff} is dependent on the diameter, and the phase delay can be obtained as $\varphi = k_0 n_{eff} H$, where the changing n_{eff} results in φ modulation[46]. From this equation, we also know that the height of dielectric micropillar H would also influence the phase delay. Figure 2(h) shows the electromagnetic field from a unit cell with a micropillar from the design library. We observe that the transmitted light from micropillar with a larger diameter has a greater phase delay, confirming the phase manipulation capability of diameter-modulated micropillars. It should be noted that the electric field is mainly concentrated inside the micropillars, and the coupling between neighboring unit cells could be neglected, indicating each micropillar could locally tune the phase with the unit cell area.

The wavefront could be effectively controlled by arranging micropillars with different phase delaying capa-

bilities. Figure 3(a) shows a plane wave normally incident on an array of micropillars arranged from left to right with each having a phase delay ranging from 0 to 7π/4 with a π/4 increment. In the region with $z < 0$ lies the As$_2$Se$_3$ substrate, and the region with $z > 0$ has As$_2$Se$_3$ micropillars embedded in air, emulating the actual working environment of metasurface. We could observe that the transmitted light deviates by approximately 13° from the normal direction, agreeing well with the theoretical deflection angle (12.84°) calculated from the generalized Snell's law[25].

Metalens transforms a plane wavefront into a converging one, where the required phase delay can be described as a hyperbolic function as

$$\varphi(x, y) = \frac{2\pi}{\lambda}\left(f - \sqrt{x^2 + y^2 + f^2}\right), \qquad (1)$$

where x and y are Cartesian coordinates with their origin located in the center of the metalens, φ is the phase
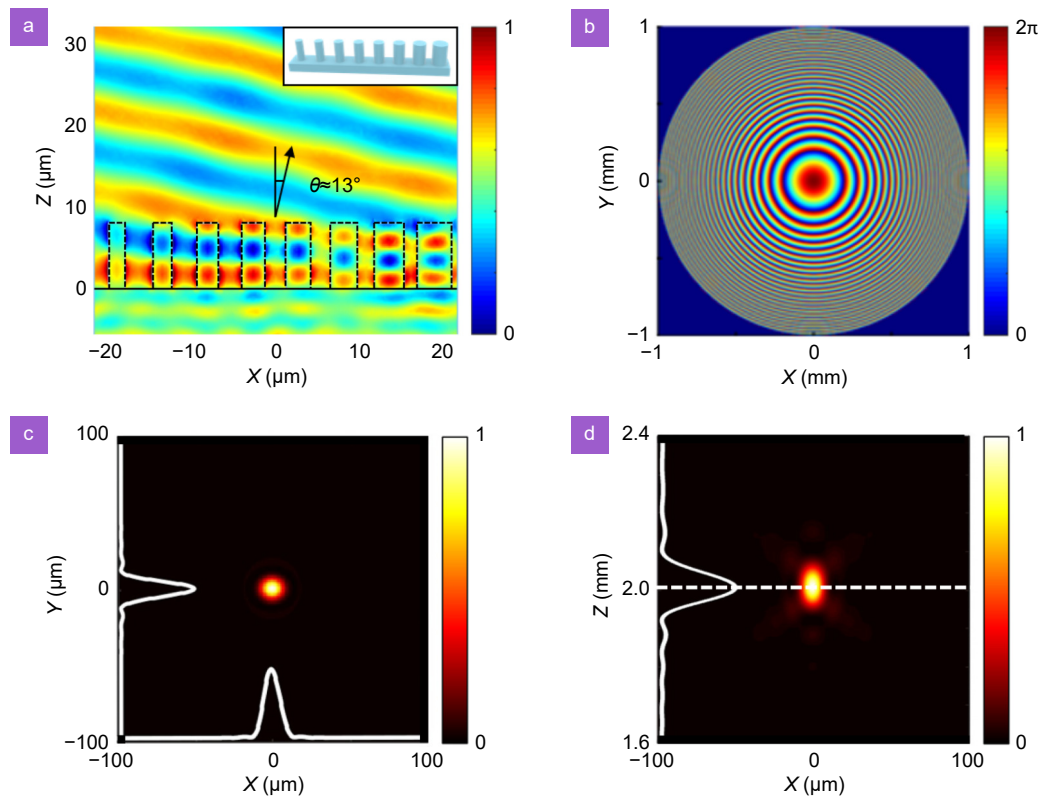
Fig. 3 | (a) Transmitted field profile through a beam deflecting metasurface with a deflection angle θ of 13°. **(b)** The discrete phase profile of an all-As_2Se_3 metalens with a diameter of 2 mm. **(c)** The intensity distribution of the light field on the *x-y* plane at the focal plane of the designed metalens. **(d)** Simulation of the normalized field intensity profile on the *x-z* plane at *y* = 0 µm after light passes through the metalens, concentrating incident light at the focal point with *z* = 2 mm.

delay at position (x, y), λ represents the working wavelength in free space, and f denotes the focal length. We aim to realize an all-chalcogenide LWIR metalens with an aperture diameter of 2 mm and focal length of 2 mm, corresponding to a numerical aperture (NA) of 0.45. In such a case, the chosen period is sufficiently small to meet the Nyquist sampling criterion, i.e. $P < \lambda/(2NA)$[46,47]. Figure 3(b) shows the wrapped phase profile of the designed metalens. Owing to the rotational symmetry of the phase profile with respect to the metalens center, we could pick the parameter of the unit cell in the square lattice according to the distance to the center. We carried out a full wave simulation based on the finite difference time domain method to simulate the focusing properties of the designed metalens. Figure 3(c) shows the normalized electric field distribution (in the *x-y* plane) at the focal plane, and the FWHM of the focal spot is 11.9 µm, closing to the diffraction limit. Figure 3(d) shows the propagating focusing electric field along *x-z* plane at *y* = 0 µm. The incident light is tightly focused near *z* = 2 mm, confirming the validity of the design procedure.

Fabrication of the LWIR As₂Se₃ metalens

Figure 4(a) shows the schematics of the fabrication process of all-chalcogenide glass metalens. Initially, the homemade As_2Se_3 glass was cut, and polished, to ensure the parallelism of two sides. The As_2Se_3 glass disks have a diameter of 10 mm and a thickness of 1.5 mm.

The high-aspect-ratio As_2Se_3 micropillars require a deep etching process. On the prepared As_2Se_3 glass disks, we first spin-coat a photoresist film which is then baked and exposed by electron beam lithography (Raith eLINE Plus) to generate a negative metalens pattern. Subsequently, a chromium (Cr) layer with a thickness of 100 nm is deposited on the patterned photoresist film which was sequentially removed by an N-methyl-2-pyrrolidone (NMP) solution, leaving only the Cr pattern on the substrate. The As_2Se_3 glass disk with Cr hard mask is then etched with trifluoromethane and tetrafluoromethane (CHF_3 and CF_4) plasma until the etch depth reaches ~8 µm. For removing the residual Cr, we chose a hydrochloric acid solution, because common chromium removal solutions have strong oxidation properties, which would react with As_2Se_3 glass. For better Cr
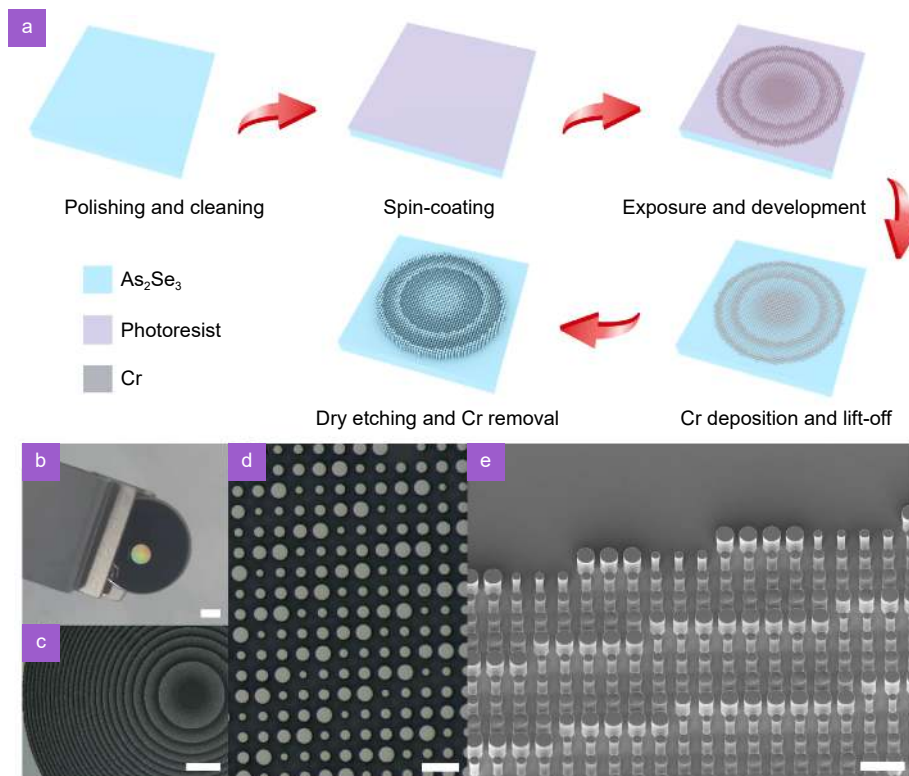
Fig. 4 | (**a**) Fabrication process of the all-chalcogenide glass metalens. The metalens is fabricated using a selective etching process. Initially, the photoresist is patterned using an electron beam exposure system. Following development, chromium (Cr) is deposited and the resist is removed. Subsequently, the As$_2$Se$_3$ glass undergoes dry etching with fluoride gas utilizing the Cr pattern as an etching mask. Cr exhibits low etching rates in fluoride plasma. Upon reaching an etched column height of 8 μm, the etching process is terminated, and the structure is immersed in a hydrochloric acid solution to dissolve the metal mask, leaving only the As$_2$Se$_3$ micropillar structure. (**b**) Photograph of the fabricated 2 mm diameter metalens on the surface of a As$_2$Se$_3$ glass disk with a diameter of 10 mm. Scale bar: 2 mm. (**c**) and (**d**) These images depict metalens captured under Olympus microscopes at different magnifications, with scale bars of 200 μm and 10 μm, respectively. (**e**) A zoomed-in view of the metalens captured by SEM. Scale bar: 10 μm.

removals, depositing a thin layer of aluminum before Cr could accelerate the hard mask removal speed. Figure 4(b) shows the photograph of an entire fabricated 10 mm-diameter chalcogenide glass disk with a 2-mm-diameter metalens structure on its surface. Microscope images (Olympus, BX51M) show the etched micropillars have a favorable morphology, as depicted in Fig. 4(c, d). Figure 4(e) presents a tilted scanning electron microscope (SEM) image of the fabricated metalens at the edge, showing a nearly vertical sidewall of micropillars. Note that owing to the soft and brittle mechanical properties of chalcogenide material, we need to optimize multiple etching parameters in order to achieve micropillars with vertical sidewalls and precisely controlled diameters (fabrication details are described in the *Materials and Methods* section).

Characterization of the LWIR As$_2$Se$_3$ metalens

To quantify the quality of the fabricated metalens, we perform various characterizations including focal length, focusing efficiency, imaging resolution and temperature-dependent focusing performances. Figure 5(a) depicts the schematic of the measurement setup. A quantum cascaded laser (QCL, Ningbo Healthy Photon Co., Ltd, QC-Qube) emits a collimated beam at 9.78 μm LWIR light to illuminate the metalens from the substrate side. The transmitted light is collected by a reflective objective lens (ROL, Thorlabs, LMM-15XF-P01-160), and then directed into infrared focal plane arrays (FPA, IRay Technology Co., Ltd, M3640) for imaging the focal spot. The FPA has a resolution of 640×512 with a pixel size of 12 μm × 12 μm. The FPA and ROL are sitting on a translational stage (Newport, M-462-XYZ-M). The measured intensity profiles at various distances (Δz) near the focal plane are depicted in Fig. 5(b), and the obtained focal length is 2 mm ± 30 μm, which agrees well with the design.
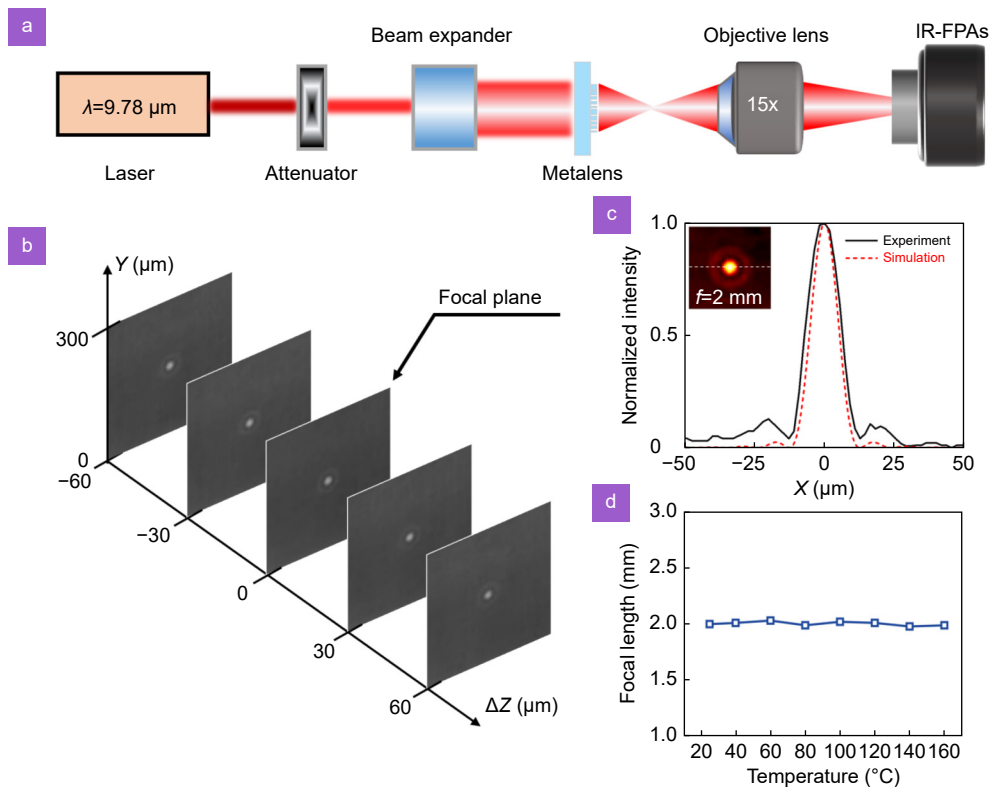
Fig. 5 | (a) The measurement setup utilized to characterize the focusing performance of the fabricated metalens. **(b)** Intensity profiles (*x-y* cross-section) measured at various distances (Δ*z*) from the focal plane. **(c)** Cross-sectional views of the normalized light intensity profiles (represented by the black line) and calculated intensity profiles (represented by the red dotted line) along the *x*-axis direction on the focal plane. The inset is a focus image of the metalens. **(d)** Focal length of metalens at different temperatures.

Figure 5(c) shows the intensity distribution at the focal plane, and the inset shows the focal beam spot. To quantitatively assess the beam spot on the focal plane, the cross sections of the normalized experimental and simulated intensity profiles along the *x*-axis direction are plotted, as shown in Fig. 5(c). The simulation results indicate that the full-width at half-maximum (FWHM) of the focus is 11.9 μm, aligning closely with the theoretical diffraction limit formula ($0.514\lambda/NA$), which approximates 11.2 μm. Note that the fabricated all-chalcogenide glass metalens with a diameter of 2 mm and a focal length of 2 mm, corresponding to a NA of ~0.45. The measured actual FWHM at the focal point slightly exceeds this at 13.6 μm.

LWIR camera may work in extreme environment, such as high ambient temperature. Common germanium-based LWIR lenses would have a degraded imaging performance due to increased optical loss induced by thermally generated holes when temperature rises above 100 °C. As_2Se_3 glass has a temperature coefficient of refractive index ($dn/dt = ~32 \times 10^{-6}/K$), nearly one order of magnitude lower than that of germanium, which promis-

es better thermal stability against large temperature variation. Figure 5(d) illustrates the focal length of the all-chalcogenide glass metalens under different ambient temperatures. With increasing temperature ($< T_g \approx 189$ °C) of the all-chalcogenide metalens, the focal length remains nearly constant, where small fluctuations may be caused by measurement inaccuracies.

Then, we characterize the focusing efficiency of fabricated metalens. The focusing efficiency is measured as the ratio of the light power passing through a pinhole with a 50 μm diameter (Thorlabs, P50HK) around the focal point to the total light power incident on the 2-mm-diameter metalens area. We observe a periodic variation of transmitted light power (~50%) with respect to wavelength shifting of QCL induced by injecting current, due to the Fabry-Perot (F-P) interference occurring in the As_2Se_3 substrate. The F-P interference also leads to a sharp variation in transmitted light power with a slight change of the incident angle. In this case, it is difficult to determine the actual focusing efficiency. To mitigate this effect, we deposit an antireflection coating on the back-side of the metalens, to suppress the reflection on the

smooth side of As_2Se_3 disk (See Supplementary information for detail). The measured focusing efficiency is 47% at a wavelength of 9.780 μm, which is lower than the theoretical value of 58%. This discrepancy may be attributed to surface contamination, or manufacturing errors.

Figure 6(a) displays the USAF-1951 resolution test chart and its image captured by the as-fabricated all-chalcogenide metalens, where the test chart is placed at a distance of 2*f* from the metalens. The smallest observable feature in the resolution test chart exhibits a line width of 31 μm, equivalent to 16.1 line pairs per millimeter (lp/mm). Figure 6(b) shows the high-temperature electric soldering iron imaged by the metalens without and with a narrow bandpass filter (Thorlabs, FB10000-500, 10 μm center wavelength, 0.5 μm FWHM). We could observe the broadband thermal emission from the soldering iron result in a blurry image on the edge, due to chromatic aberration, while the bandpass filter could improve the image quality with a sharper edge. Figure 6(c) and 6(d) shows the NBU logo on a polymer disk illuminated by a blackbody irradiation and a human hand imaged by the all-chalcogenide metalens.

Discussion

It is worth mentioning that despite their exceptional optical performance in the LWIR range, chalcogenide materials typically exhibit low mechanical strength and poor stability against humidity and environmental influences, which can negatively impact the long-term durability of all-chalcogenide metalenses. These drawbacks can be mitigated by using functional protective anti-reflection coatings, such as diamond-like carbon films[48], which possess excellent mechanical properties and high corrosion resistance. These coatings can be further exploited to enhance the resilience of chalcogenide materials.

Table 1 summarize previously reported all-dielectric metalenses working in LWIR range. We observe that a heterogeneous Si/BaF_2 metalens (ref.[53]) have a focusing efficiency of ~72%, attributed to reduced reflection loss resulted from low index BaF_2 substrate (~1.4). In contrast, homogeneous metalenses based on silicon or germanium exhibit much lower focusing efficiencies, around 30%. Notably, the all-Si metalens reported in ref.[56] demonstrates a focusing efficiency of 64.94% with a low NA (0.1) design. Another trend observed is that all-Ge metalenses have a lower focusing efficiency of ~20.5% owing to a higher reflection loss. Compared with previous works summarized in Table 2, the all-chalcogenide (As_2Se_3) metalens shows improved focusing efficiency due to its excellent transmission and moderate refractive index (~2.78) within the LWIR range. Recently, we have noticed that ultra-flat lenses made from 2D materials offer an intriguing platform for efficient light field manipulation. Exploring LWIR imaging using atomically-thin 2D materials-based metalenses provides a novel avenue for further reducing the volume of infrared optical lenses[49−52].

In our work, the measured focusing efficiency of all-chalcogenide metalens is 47%. This value could be further improved by using antireflection coating on the structured side, which required a joint consideration of phase control and reflection reduction in the microstructure
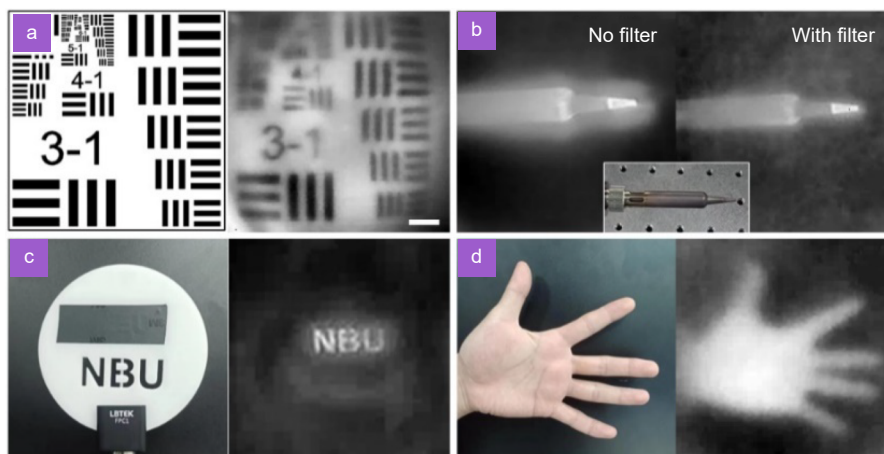
Fig. 6 | (a) The target resolution test chart (left), and the captured image of a resolution card (right) by all-chalcogenide metalens under blackbody radiation with a narrow bandpass filter. Scale bar: 200 μm. **(b)** The image of the high-temperature electric soldering iron captured by the metalens without (left) and with (right) the narrow bandpass filter. The inset is the photograph of soldering iron. **(c)** A polymer NBU logo and its image under blackbody irradiation with a narrowband filter. **(d)** The thermal image of a human hand captured by the all-chalcogenide metalens.

Table 2 | Performance comparison of all-dielectric metalenses working in LWIR range.

Ref.	Material	Aperture size	Wavelength	Focal spot size	N.A.	Efficiency
ref.[29]	Si	12 mm	10.6 μm	~1.08λ	0.6	35%
ref.[53]	Si/BaF$_2$	8 mm	10.6 μm	1.25λ/5.85λ	~0.45	72%
ref.[35]	Si	0.1 mm×0.1 mm	10.6 μm	~1.2λ	~0.45	~34%
ref.[54]	Si	0.2 mm	8.5–11.5 μm	~1.68λ (@10 μm)	0.33	~10%
ref.[55]	Si	6 mm	10 μm	~0.89λ	0.81	~24%
ref.[56]	Si	30 mm×30 mm	10.6/9.3 μm	~5.26λ	~0.1	64.94%
ref.[57]	Ge	12.2 mm	8–12 μm	Not reported	~0.38	20.5% (@9.3 μm)
This work	As$_2$Se$_3$	2 mm	9.78 μm	1.39λ	0.45	47%

design. We believe a multilayer microstructure metalens could help to achieve this goal[58,59]. In addition, optimizing the diffraction efficiency at the peripheral region of high-NA metalenses offers a promising route to further improve the focusing efficiency[60−63].

Conclusions

In summary, we have established a new route to monolithically integrate metasurface on chalcogenide glass by directly pattern glass surface with high-aspect-ratio microstructures. With an optimized fabrication process, we successfully fabricate large-aspect-ratio micropillars with a height of 8 μm and varying diameters on the surface of As$_2$Se$_3$ glasses. The as-fabricated 2-mm-aperture all-chalcogenide metalenses could efficiently focus LWIR light with a focal spot FWHM of 1.39λ_0, closing to the diffraction limit. We also found homogenous metalens (i.e. microstructure and substrate made of the same materials) may be subject to strong transmission efficiency variation due to Fabry-Perot resonances in the substrate. By implementing an anti-reflection layer on the backside of the metalens, the measured focusing efficiency is 47%, while the theoretical value is 58%. Owing to the material properties of As$_2$Se$_3$ glasses, the fabricated metalens demonstrate good imaging performances, and stable focusing feature under varying ambient temperatures. Our work provides a new paradigm for realizing ultracompact, high-efficiency infrared optics using surface-patterned chalcogenide glass, which offers great potential for LWIR imaging systems applied in autonomous driving, airborne surveillance, personal night vision, and other weight-sensitive applications.

Materials and methods

Simulations: We perform numerical simulation to obtain the optical response of metalens unit cell using Lumerical FDTD solver. The refractive index of chalcogenide glass (As$_2$Se$_3$) is 2.78, since As$_2$Se$_3$ has very low dispersion in LWIR frequencies. The square unit cell is embedded in air with a refractive index of 1. Periodic boundary conditions are imposed in the *x-y* plane. Plane wave source polarized along *x*-axis is injected to excite the unit cell. To obtain the transmittance and phase as a function of pillar height and unit cell period, we employ a MATLAB-based RCWA solver (Reticolo) to perform the calculation, and two methods show good consistency. The focusing performance of the all-chalcogenide metalens is simulated by Lumerical FDTD solver, and near-to-farfield transformation is utilized to obtain the focal spot field profile as well as focusing efficiency.

Fabrication: We pre-baked the chalcogenide glass disk at 150 °C for 10 min, then spin coated positive e-beam resists AR-P 6200.09 (Allresist) with a thickness of 200 nm and bake it under 150 °C hot plate for 8-min. Then spin coating 42 nm thick protective coating AR-PC 5090.02 (Allresist) for the dissipation of e-beam charges on insulating substrates and bake at 105 °C hot plate for 5-min. In all high temperature steps, there are 70 °C of hot plate insulation for 2 min after high temperature baking, in order to prevent glass substrate cracking. The 2 mm metalens pattern was written by 30 kV electron beam lithography (Raith eLINE Plus). After exposure, the conductive coating was removed by soaking in deionized water for 30 s, then developed with AR 600-546 developer (Allresist) for 1 min, fixed with IPA for 30 s, and baked on a 130 °C hot plate for 1 min. Then, the samples were brought into the sputtering chamber (Lesker, PVD 75) and a chromium (Cr) layer with a thickness of 100 nm is deposited on the patterned photoresist film which was sequentially removed by an N-methyl-2-pyrrolidone (NMP) solution, leaving only the Cr pattern on the substrate. The As$_2$Se$_3$ glass disk with Cr hard mask is then etched by inductively coupled plasma (ICP, Oxford Instruments, PlasmaPro 100 Cobra

180) with trifluoromethane and tetrafluoromethane plasma (CHF_3:CF_4 = 20/10 sccm, 6 mTorr) until the etch depth reaches ~8 μm. For removing the residual Cr, we chose a hydrochloric acid solution, because common chromium removal solutions have strong oxidation properties, which would react with As_2Se_3 glass. For better Cr removals, depositing a thin layer of aluminum before Cr could accelerate the hard mask removal speed.

Measurement: The light at the focal spot is collected through a reflective objective (ROL, Thorlabs, LMM-15XF-P01-160) and then guided to an infrared focal plane array (FPA, IRay Technology Co., Ltd., M3640) to obtain a focal spot image. The FPA resolution is 640×512 and the pixel size is 12 μm × 12 μm. FPA and ROL are fixed on a translational stage (Newport, M-462-XYZ-M). The light source is a quantum cascade laser (QCL, Ningbo Healthy Photon Co., Ltd, QC-Qube), which emits collimated LWIR light at 9.78 μm, and the spot size is expanded by a mid-IR Galilean beam expander (Thorlabs, GBE10-E3). The focusing efficiency is measured as the ratio of the light power passing through a pinhole with a 50 μm diameter (Thorlabs, P50HK) around the focal point to the total light power incident on the 2-mm-diameter metalens area. For the imaging tests, both the US-AF-1951 resolution test pattern and the NBU letter pattern are irradiated by a blackbody reference sources (CEM, BX-500), and the light passing through the pattern is then captured by the as-fabricated all-chalcogenide metalens after passing through a narrow bandpass filter (Thorlabs, FB10000-500, 10 μm center wavelength, 0.5 μm FWHM). The images produced by the metalens are collected through the reflective objective (ROL, Thorlabs, LMM-15XF-P01-160), and then guided to the uncooled thermal imaging module (IRay Technology Co., Ltd., M3S6) to obtain the final image.

References

1. Eggleton BJ, Luther-Davies B, Richardson K. Chalcogenide photonics. *Nat Photon* **5**, 141–148 (2011).
2. Bernier M, Fortin V, Caron N et al. Mid-infrared chalcogenide glass Raman fiber laser. *Opt Lett* **38**, 127–129 (2013).
3. Zhao ZM, Wu B, Wang XS et al. Mid-infrared supercontinuum covering 2.0–16 μm in a low-loss telluride single-mode fiber. *Laser Photonics Rev* **11**, 1700005 (2017).
4. Ta'eed VG, Baker NJ, Fu LB et al. Ultrafast all-optical chalcogenide glass photonic circuits. *Opt Express* **15**, 9205–9221 (2007).
5. Su P, Han Z, Kita D et al. Monolithic on-chip mid-IR methane gas sensor with waveguide-integrated detector. *Appl Phys Lett* **114**, 051103 (2019).
6. Kang M, Sisken L, Lonergan C et al. Monolithic chalcogenide optical nanocomposites enable infrared system innovation: gradient refractive index optics. *Adv Opt Mater* **8**, 2000150 (2020).
7. Zheng WF, Xia KL, Jia G et al. Customized linear refractive index GRIN prepared by rapid sintering of multilayer chalcogenide glass powders. *J Am Chem Soc* **107**, 4585–4593 (2024).
8. Gibson D, Bayya S, Nguyen V et al. IR-GRIN optics for imaging. *Proc SPIE* **9822**, 98220R (2016).
9. Zhang XH, Guimond Y, Bellec Y. Production of complex chalcogenide glass optics by molding for thermal imaging. *J Non-Cryst Solids* **326–327**, 519–523 (2003).
10. Ostrovsky N, Yehuda D, Tzadka S et al. Direct imprint of optical functionalities on free-form chalcogenide glasses. *Adv Opt Mater* **7**, 1900652 (2019).
11. Deng HT, Qi DF, Wang XM et al. Femtosecond laser writing of infrared microlens arrays on chalcogenide glass. *Opt Laser Technol* **159**, 108953 (2023).
12. Arbabi A, Horie Y, Bagheri M et al. Dielectric metasurfaces for complete control of phase and polarization with subwavelength spatial resolution and high transmission. *Nat Nanotechnol* **10**, 937–943 (2015).
13. Guo YH, Zhang SC, Pu MB et al. Spin-decoupled metasurface for simultaneous detection of spin and orbital angular momenta via momentum transformation. *Light Sci Appl* **10**, 63 (2021).
14. Zhu RC, Wang JF, Qiu TS et al. Direct field-to-pattern monolithic design of holographic metasurface via residual encoder-decoder convolutional neural network. *Opto-Electron Adv* **6**, 220148 (2023).
15. Fan JX, Li ZL, Xue ZQ et al. Hybrid bound states in the continuum in terahertz metasurfaces. *Opto-Electron Sci* **2**, 230006 (2023).
16. Wang K, Titchener JG, Kruk SS et al. Quantum metasurface for multiphoton interference and state reconstruction. *Science* **361**, 1104–1108 (2018).
17. Xu DY, Xu WH, Yang Q et al. All-optical object identification and three-dimensional reconstruction based on optical computing metasurface. *Opto-Electron Adv* **6**, 230120 (2023).
18. Zhang F, Guo YH, Pu MB et al. Meta-optics empowered vector visual cryptography for high security and rapid decryption. *Nat Commun* **14**, 1946 (2023).
19. Luo XG. Principles of electromagnetic waves in metasurfaces. *Sci China Phys Mech Astron* **58**, 594201 (2015).
20. Yue Z, Li JT, Li J et al. Terahertz metasurface zone plates with arbitrary polarizations to a fixed polarization conversion. *Opto-Electron Sci* **1**, 210014 (2022).
21. Park JS, Zhang SY, She AL et al. All-glass, large metalens at visible wavelength using deep-ultraviolet projection lithography. *Nano Lett* **19**, 8673–8682 (2019).
22. Lalanne P, Chavel P. Metalenses at visible wavelengths: past, present, perspectives. *Laser Photonics Rev* **11**, 1600295 (2017).
23. Wang YJ, Chen QM, Yang WH et al. High-efficiency broadband achromatic metalens for near-IR biological imaging window. *Nat Commun* **12**, 5560 (2021).

24. Zuo HJ, Choi DY, Gai X et al. High-efficiency all-dielectric metal-enses for mid-infrared imaging. *Adv Opt Mater* **5**, 1700585 (2017).

25. Yoon G, Kim K, Kim SU et al. Printable nanocomposite metal-ens for high-contrast near-infrared imaging. *ACS Nano* **15**, 698–706 (2021).

26. Zhang F, Pu MB, Li X et al. Extreme-angle silicon infrared optics enabled by streamlined surfaces. *Adv Mater* **33**, 2008157 (2021).

27. Zhang SY, Soibel A, Keo SA et al. Solid-immersion metalenses for infrared focal plane arrays. *Appl Phys Lett* **113**, 111104 (2018).

28. Lim SWD, Meretska ML, Capasso F. A high aspect ratio inverse-designed holey metalens. *Nano Lett* **21**, 8642–8649 (2021).

29. Fan QB, Liu MZ, Yang C et al. A high numerical aperture, polarization-insensitive metalens for long-wavelength infrared imaging. *Appl Phys Lett* **113**, 201104 (2018).

30. Hou MM, Chen Y, Yi F. Lightweight long-wave infrared camera via a single 5-centimeter-aperture metalens. In *2022 Conference on Lasers and Electro-Optics* 1–2 (IEEE, 2022). https://ieeexplore.ieee.org/abstract/document/9890320

31. Lin HI, Geldmeier J, Baleine E et al. Wide-field-of-view, large-area long-wave infrared silicon metalenses. *ACS Photonics* **11**, 1943–1949 (2024).

32. Soref RA, Emelett SJ, Buchwald WR. Silicon waveguided components for the long-wave infrared region. *J Opt A Pure Appl Opt* **8**, 840–848 (2006).

33. Wang A, Chen ZM, Dan YP. Planar metalenses in the mid-infrared. *AIP Adv* **9**, 085327 (2019).

34. Nalbant HC, Balli F, Yelboğa T et al. Transmission optimized LWIR metalens. *Appl Opt* **61**, 9946–9950 (2022).

35. Liu MZ, Fan QB, Yu L et al. Polarization-independent infrared micro-lens array based on all-silicon metasurfaces. *Opt Express* **27**, 10738–10744 (2019).

36. Palik ED. *Handbook of Optical Constants of Solids: Volume 2* (Academic Press, Orlando, 1991).

37. Lipson HG, Tsay YF, Bendow B et al. Temperature dependence of the refractive index of alkaline earth fluorides. *Appl Opt* **15**, 2352–2354 (1976).

38. Hahn D. Calcium fluoride and barium fluoride crystals in optics. *Opt Photonik* **9**, 45–48 (2014).

39. Palik ED. *Handbook of Optical Constants of Solids* (Academic Press, Orlando, 1998).

40. Palik ED. *Handbook of Optical Constants of Solids: Volume 1* (Academic Press, Orlando, 1985).

41. Harris RJ, Johnston GT, Kepple GA et al. Infrared thermooptic coefficient measurement of polycrystalline ZnSe, ZnS, CdTe, CaF_2, and BaF_2, single crystal KCl, and TI-20 glass. *Appl Opt* **16**, 436–438 (1977).

42. Valdez LA, Caravaca MA, Casali RA. Ab-initio study of elastic anisotropy, hardness and volumetric thermal expansion coefficient of ZnO, ZnS, ZnSe in wurtzite and zinc blende phases. *J Phys Chem Solids* **134**, 245–254 (2019).

43. Icenogle HW, Platt BC, Wolfe WL. Refractive indexes and temperature coefficients of germanium and silicon. *Appl Opt* **15**, 2348–2351 (1976).

44. Batchelder DN, Simmons RO. Lattice constants and thermal expansivities of silicon and of calcium fluoride between 6° and 322°K. *J Chem Phys* **41**, 2324–2329 (1964).

45. Harris DC. Durable 3–5 μm transmitting infrared window materials. *Infrared Phys Technol* **39**, 185–201 (1998).

46. Khorasaninejad M, Zhu AY, Roques-Carmes C et al. Polarization-insensitive metalenses at visible wavelengths. *Nano Lett* **16**, 7229–7234 (2016).

47. Chen WT, Zhu AY, Khorasaninejad M et al. Immersion metalenses at visible wavelengths for nanoscale imaging. *Nano Lett* **17**, 3188–3194 (2017).

48. Lee JH, Kim H, Lee WH et al. Surface modification of chalcogenide glass for diamond-like-carbon coating. *Appl Surf Sci* **478**, 802–805 (2019).

49. Lin H, Xu ZQ, Cao GY et al. Diffraction-limited imaging with monolayer 2D material-based ultrathin flat lenses. *Light Sci Appl* **9**, 137 (2020).

50. Zheng XR, Jia BH, Lin H et al. Highly efficient and ultra-broadband graphene oxide ultrathin lenses with three-dimensional subwavelength focusing. *Nat Commun* **6**, 8433 (2015).

51. Wang HT, Hao CL, Lin H et al. Generation of super-resolved optical needle and multifocal array using graphene oxide metalenses. *Opto-Electron Adv* **4**, 200031 (2021).

52. Cao GY, Lin H, Jia BH. Broadband diffractive graphene orbital angular momentum metalens by laser nanoprinting. *Ultrafast Sci* **3**, 0018 (2023).

53. Fan QB, Wang YL, Liu MZ et al. High-efficiency, linear-polarization-multiplexing metalens for long-wavelength infrared light. *Opt Lett* **43**, 6005–6008 (2018).

54. Xia CS, Liu MZ, Wang JM et al. A polarization-insensitive infrared broadband achromatic metalens consisting of all-silicon anisotropic microstructures. *Appl Phys Lett* **121**, 161701 (2022).

55. Wang YL, Zhang S, Liu MZ et al. Compact meta-optics infrared camera based on a polarization-insensitive metalens with a large field of view. *Opt Lett* **48**, 4709–4712 (2023).

56. Xu P, Li XC, Yang T et al. Long-infrared dual-wavelength linear-polarization-multiplexed confocal metalens based on an all-silicon dielectric. *Opt Express* **31**, 26685–26696 (2023).

57. Hu T, Wen L, Li H et al. Aberration-corrected hybrid metalens for longwave infrared thermal imaging. *Nanophotonics* **13**, 3059–3066 (2024).

58. Basilio-Ortiz JC, Moreno I. Multilayer dielectric metalens. *Opt Lett* **47**, 5333–5336 (2022).

59. Basilio-Ortiz JC, Moreno I. All dielectric reflective metalens based on multilayer meta-atoms. *Opt Lett* **48**, 5647–5650 (2023).

60. Chen WT, Park JS, Marchioni J et al. Dispersion-engineered metasurfaces reaching broadband 90% relative diffraction efficiency. *Nat Commun* **14**, 2544 (2023).

61. Yang MY, Shen X, Li ZP et al. High focusing efficiency metalens with large numerical aperture at terahertz frequency. *Opt*

Lett **48**, 4677–4680 (2023).

62. Phan T, Sell D, Wang EW et al. High-efficiency, large-area, topology-optimized metasurfaces. *Light Sci Appl* **8**, 48 (2019).

63. Li SY, Lin HC, Hsu CW. High-efficiency high-numerical-aperture metalens designed by maximizing the efficiency limit. *Optica* **11**, 454–459 (2024).

Acknowledgements

Author contributions

YX Gao, ZF Gu and X Shen developed the idea. ZF Gu and X Chen fabricated the devices. ZF Gu, YX Gao constructed the experimental setup, and characterized device performance. KS Zhou, JY Ge, and YX Gao conducted full-wave simulations to design the devices. ZF Gu, JY Ge, and YX Gao analyzed the data with contribution from YG Ma and L Xu. YX Gao, ZF Gu, L Xu, M Rahmani, R Jiang, YM Chen, ZJ Liu, CJ Gu, YG Ma, JR Qiu and X Shen discussed the results. YX Gao and ZF Gu wrote the manuscript with input from all authors. YX Gao and X Shen led the project.

Competing interests

The authors declare no competing financial interests.

Supplementary information

Supplementary information for this paper is available at
https://doi.org/10.29026/oes.2024.240017

Scan for Article PDF